Batteries & Supercaps

Research Article
doi.org/10.1002/batt.202200058

Chemistry
Europe
European Chemical
Societies Publishing

www.batteries-supercaps.org

Special Collection

Impact of Compression on the Electrochemical Performance of the Sulfur/Carbon Composite Electrode in Lithium-Sulfur Batteries

Yu-Chuan Chien,[a] He Li,[b] John Lampkin,[b] Stephen Hall,[c] Nuria Garcia-Araez,[b] William R. Brant,[a] Daniel Brandell,*[a] and Matthew J. Lacey[d]

While lithium-sulfur batteries theoretically have both high gravimetric specific energy and volumetric energy density, only its specific energy has been experimentally demonstrated to surpass that of the state-of-the-art lithium-ion systems at cell level. One major reason for the unrealized energy density is the low capacity density of the highly porous sulfur/carbon composite as the positive electrode. In this work, mechanical compression at elevated temperature is demonstrated to be an effective method to increase the capacity density of the electrode by at least 90% and moreover extends its cycle life. Distinct impacts of compression on the resistance profiles of electrodes with different thickness are investigated by tortuosity factors derived from both electrochemical impedance spectroscopy, X-ray computed tomography and kinetic analysis based on operando X-ray diffraction. The results highlights the importance of a homogeneous electrode structure highlight lithium-sulfur system.

Introduction

Lithium-sulfur (Li-S) batteries have been considered promising options for the post-lithium-ion energy storage systems due to the low cost of sulfur and the high theoretical specific energy and energy density of the system on the active materials level, 2500 $Wh\,kg^{-1}$ and 2800 $Wh\,L^{-1}$, respectively.[1–4] Considering the cell components in an ideally balanced cell, the specific energy of a Li-S cell, ~750 $Wh\,kg^{-1}$, is still substantially higher than the competing systems, such as 400 $Wh\,kg^{-1}$ for a cell composed of lithium nickel manganese cobalt oxide (NMC) and metallic Li.[1,3,5] However, the energy density of such Li-S cell, ~1000 $Wh\,L^{-1}$, is less impressive than that of a NMC–Li cell, ~1300 $Wh\,L^{-1}$.[1,3,5] The lower energy density can be attributed to the high porosity of the composite positive electrode, which usually consists of mainly activated carbon and elemental sulfur.[6] Moreover, the large void volume in the composite electrode needs to be filled by electrolyte, which also decreases the specific energy of the cell. Indeed, the electrolyte often constitutes more than 40% of the mass of a Li-S cell.[7] In practice, the energy density is further reduced by the excess in Li metal and electrolyte due to manufacturing limits and/or reaching a desired level of sulfur utilization and cycle life. For example, a commercially demonstrated Li-S cell exhibited an energy density of 300 $Wh\,L^{-1}$, lower than state-of-the-art Li-ion products, while its specific energy of 400 $Wh\,kg^{-1}$ was substantially higher than the latter.[8] In summary, the low energy density of current Li-S cells needs to be addressed for their further development.

Increasing the volumetric capacity density of the positive electrode can potentially raise both the energy density and specific energy on the cell level, as mentioned above. The main cause for the low density of a common S/C composite electrode is the high porosity of the porous carbon, whose high surface area is required to facilitate the electrochemical reactions between the dissolved reaction intermediates, lithium polysulfides (Li_2S_x, $x = 2-8$), and the insulating precipitates at the charged and discharged states, elemental sulfur and lithium sulfide (Li_2S), respectively.[6,9] Therefore, an approach to increase the capacity density is to replace the S/C composite by metal sulfides, e.g., FeS_2/FeS[10] and Mo_6S_8,[11] novel conductive compounds[12,13] or carbonaceous materials with covalently bonded sulfur,[14,15] which involve limited or no dissolved intermediates. However, the specific capacity of metal sulfides are lower on the materials level due to the comparatively low sulfur content of these materials. Although it has been proposed to introduce extra non-chemically-bonded sulfur and

[a] Dr. Y.-C. Chien, Dr. W. R. Brant, Prof. D. Brandell
Department of Chemistry – Ångström Laboratory
Uppsala University
Box 538, Lägerhyddsvägen 1, Uppsala 751 21, Sweden
E-mail: daniel.brandell@kemi.uu.se
[b] Dr. H. Li, Dr. J. Lampkin, Dr. N. Garcia-Araez
School of Chemistry
University of Southampton
Southampton SO17 1BJ, United Kingdom
[c] Dr. S. Hall
Solid Mechanics, Lund Institute of Advanced Neutron and X-ray Science (LINXS)
Lund University
Ole Römers väg 1, Lund 223 63, Sweden
[d] Dr. M. J. Lacey
Scania CV AB
Södertälje 151 87, Sweden

Special Collection *An invited contribution to a Special Collection dedicated to Lithium–Sulfur Batteries*

utilize the metal sulfides as the conductive matrix for the precipitation reactions to increase the specific capacity of the electrode, the overall sulfur content is still below 50% by mass.[10,11] Similar limits of the sulfur content can be found for sulfurized carbonaceous materials.[14,15]

A more straight-forward method to increase the capacity density of S/C composite electrodes is mechanical compression. For example, calendering, applying pressure on the electrode coating with a set of rolls, is a standard step of the electrode manufacturing process of Li-ion batteries.[16] Through controlling the pressing force and temperature, the process is utilized to reduce the porosity to an optimal value and improve the adhesion of the components.[17–19] Calendering has also been demonstrated on S/C composite electrodes with two major types of carbon matrices. Kim et al. reported that calendering at 70 °C improves the cycle life of S/C electrodes made from a carbon matrix with high specific surface area, Ketjenblack (KB).[20] Zhai et al. showed similar positive effects of compression on the cycle life of electrodes with high porosity, using carbon nanotube scaffolds.[21] Although the benefits of calendering have been concluded in both reports, the impact of compression on the transport properties inside the porous electrode was not characterized.

In this work, the impact of mechanical compression on the structure of S/C composite electrodes and their electrochemical properties are investigated, thereby highlighting the interplay between electrode structure, transport properties and the electro-

chemical performance of the cells. The compression carried out by normal stress is found to render more consistent results than calendering. The pristine and pressed electrode structures are then characterized by methods based on electrochemical impedance spectroscopy (EIS) and X-ray computed tomography (XRCT). The results from both approaches show that the increase in tortuosity caused by compression have distinct effects on the electrodes with different loadings. This discrepancy motivates the follow-up operando X-ray diffraction (XRD) experiments, which indicate that the precipitation kinetics of Li_2S are strongly suppressed in the thick compressed electrode.

Results and Discussion

After testing several experimental parameters for compressing the electrodes, we found that pressing the electrodes vertically by a hydraulic press at an elevated temperature (A photo of the setup is in Figure S1) achieved the largest degree of compres-
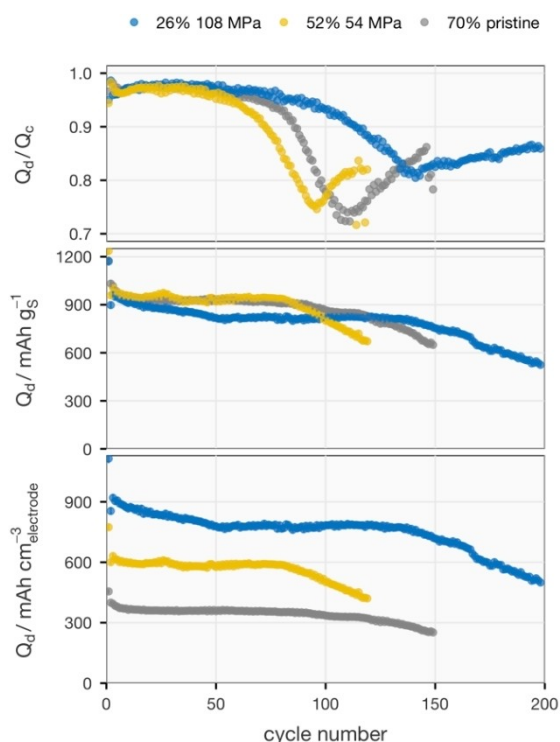

Figure 1. Coulombic efficiency (top), specific capacity (middle) and capacity density (bottom) of the pristine and compressed electrodes with a sulfur-loading of 2.0–2.5 $mg_S\,cm^{-2}$ are plotted against the cycle number. The compressed electrodes are marked with their porosity and the applied pressure. Q_d and Q_c stand for discharge and charge capacity, respectively.
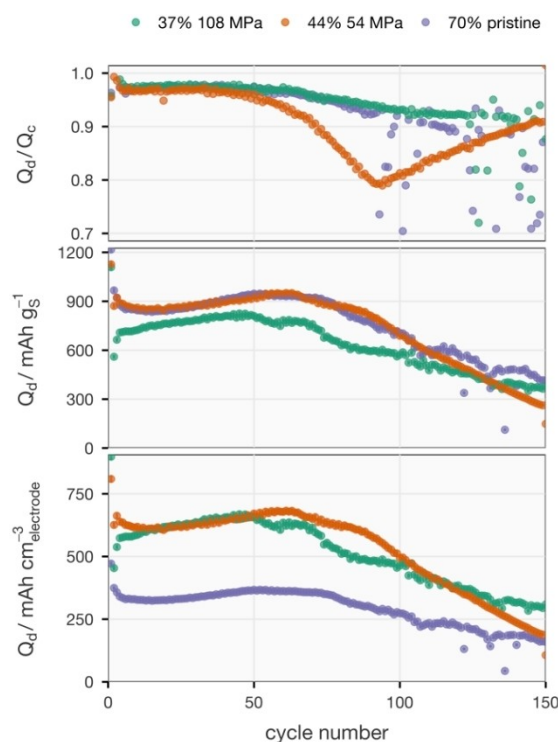

Figure 2. Coulombic efficiency (top), specific capacity (middle) and capacity density (bottom) of the pristine and compressed electrodes with a sulfur-loading of 3.0–3.5 $mg_S\,cm^{-2}$ are plotted against the cycle number. The compressed electrodes are marked with their porosity and the applied pressure. Q_d and Q_c stand for discharge and charge capacity, respectively.

Table 1. Tortuosity factors of the compressed (108 MPa) and pristine electrodes, with the lower and higher sulfur-loadings, derived from EIS and XRCT measurements.

S-loading [$mg_S\,cm^{-2}$]	From EIS		From XRCT	
	pristine	compressed	pristine	compressed
2.0–2.5	2.5	4.5	1.3	2.2
3.0–3.5	2.2	3.7	1.4	1.6

Batteries & Supercaps

Research Article
doi.org/10.1002/batt.202200058

Chemistry Europe
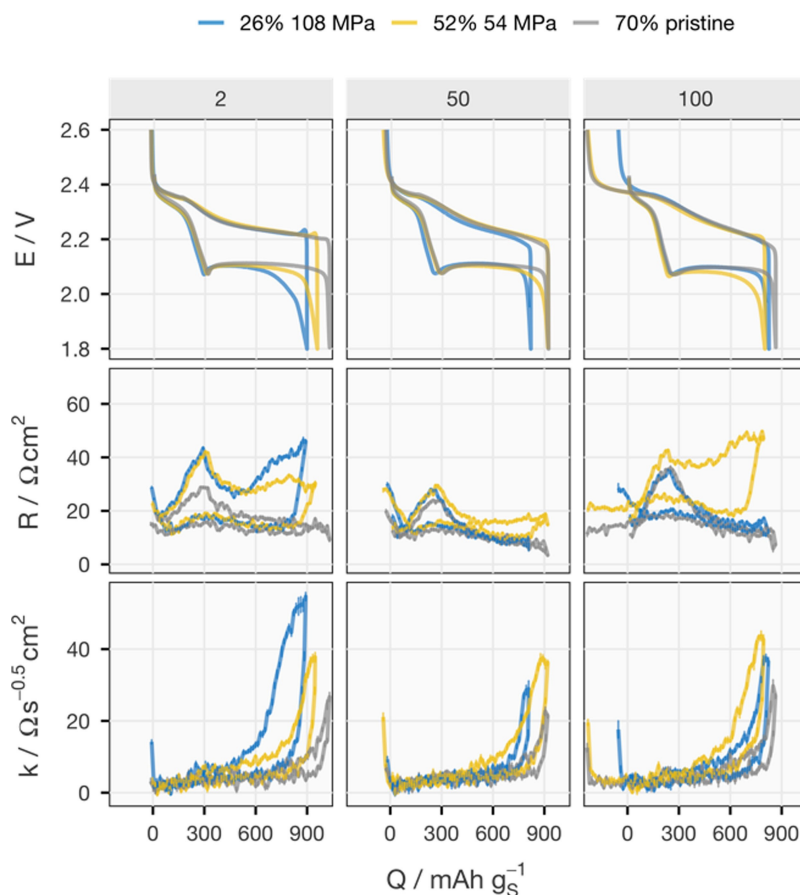European Chemical
Societies Publishing

Figure 3. Cell voltage (E), internal resistance (R) and diffusion resistance coefficient (k) of the pristine and compressed electrodes with a sulfur-loading of 2.0–2.5 $mg_S\,cm^{-2}$ in the 2nd, 50th and 100th cycles are plotted as a function of state of charge/discharge in terms of specific capacity (Q). The compressed electrodes are marked with their porosity and the applied pressure. The R and k are higher during discharging than during charging, except for the end of charging.

sion and produced the most consistent results. Therefore, the following discussions are focused on electrodes pressed at 50 °C while the results from calendering and pressing without heating are shown in Figures S2 and S3.

The cycling behavior of the compressed electrodes with a lower sulfur-loading (2.0–2.5 $mg_S\,cm^{-2}$, defined as mass of sulfur per electrode area) are illustrated in Figure 1. Two levels of pressure (108 and 54 MPa) were applied on the electrodes by a hydraulic press, which decreases the porosity substantially to 26% and 52%, respectively. As a reference for comparison, 26% is approximately the porosity of a pressed NMC electrode.[19] The decrease in porosity from 70% to 26% corresponds to an increase in electrode density from 0.6 to 1.5 g cm^{-3}, as tabulated in Table S1. Despite the slightly lowered specific capacity, the electrode pressed at 108 MPa shows extended cyclability in terms of specific capacity and higher Coulombic efficiency (CE). Interestingly, the electrode pressed at 54 MPa does not lose any specific capacity compared to the pristine electrode but has a shorter cycle life based on both capacity retention and CE. The worsened and improved cycle life of pressed electrodes with intermediate and low porosity, respectively, agrees with previous observations of the electrodes with the same carbon matrix.[20] This may indicate that there is a certain level of compression necessary

to improve the electrode structure. Nevertheless, both pressed electrodes exhibit much higher capacity density on the electrode level. By pressing the electrode at 108 MPa to reduce the porosity to 26%, the stable capacity density at the 50th cycle is increased by 118%. Repeated cells with the electrodes pressed at 108 MPa were made to confirm the increased cycle life, of which the cycling behavior can be found in Figure S4.

The CE, specific capacity and capacity density of the compressed electrodes with a higher sulfur-loading (3.0–3.5 $mg_S\,cm^{-2}$) are displayed in Figure 2. In comparison to the case with the lower sulfur-loading, a lower degree of porosity reduction is achieved at 108 MPa. Nonetheless, a similar trend in the influence of compression on the cycle life can be observed by comparing the CE, which starts to decay the earliest in the electrode pressed at 54 MPa but remained stable the longest for the electrode pressed at 108 MPa. Unlike the distinct capacity density of the thinner electrodes pressed at the two pressures, similar capacity density can be observed from the thicker electrodes compressed at both pressures in the first 50 cycles. This can be attributed to the smaller difference in porosity between electrodes pressed at 54 and 108 MPa and the lower specific capacity of the latter. Nevertheless, their capacity density exhibits a 90% increase from the pristine electrode.
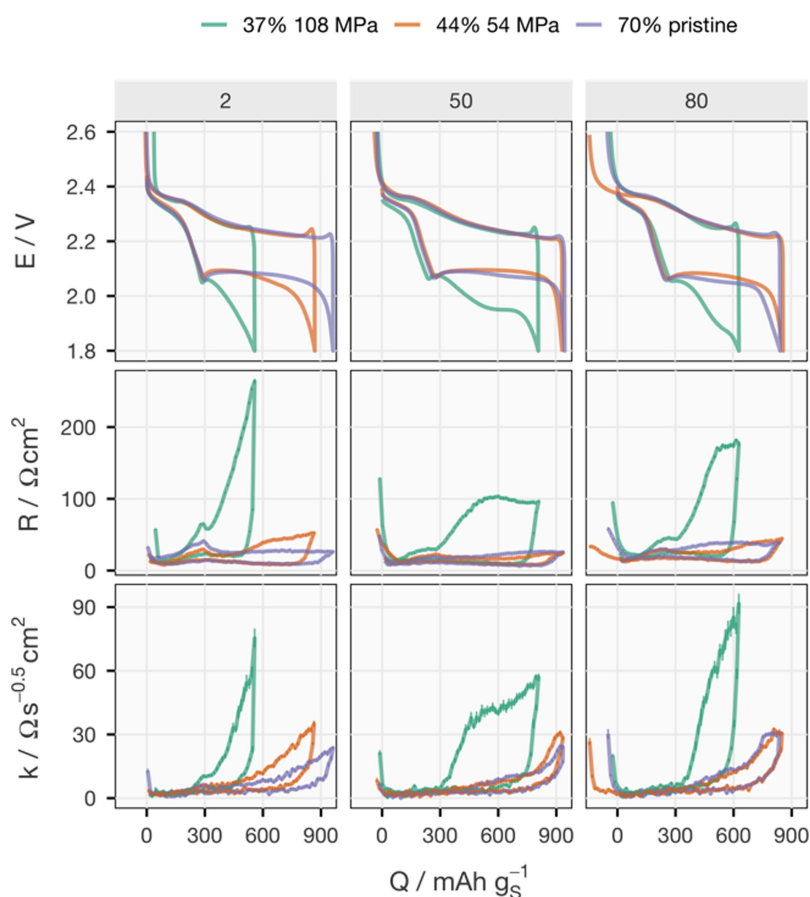
Figure 4. Cell voltage (E), internal resistance (R) and diffusion resistance coefficient (k) of the pristine and compressed electrodes with a sulfur-loading of 3.0–3.5 $mg_S\,cm^{-2}$ in the 2nd, 50th and 80th cycles are plotted as a function of state of charge/discharge in terms of specific capacity (Q). The compressed electrodes are marked with their porosity and the applied pressure. The R and k are higher during discharging than during charging, except for the end of charging.

The effects of porosity reduction on the electrochemical properties of the S/C composite electrodes with the lower sulfur-loading is illustrated in Figure 3. In cycle 2, on the lower discharge plateau, the increase in both internal and diffusion resistances agree with the increase in the degree of compression. The compressed carbon matrices are expected to be more affected by the formation of insulating Li_2S on the lower plateau due to their lower porosity. Previous XRD studies reported that the precipitation both passivates the conductive electrode surface area and deteriorates the transport properties inside the porous electrode, which increase the charge-transfer resistance (included in the internal resistance), and the diffusion resistance of the electrode, respectively.[22] Another influence of compression is the increase in the internal resistance between the upper and lower discharge plateaus in cycle 2, which indicates that the compact electrode structure is more affected by the solution resistance increase brought by the dissolution of polysulfides.[23]

The above-mentioned effects of mechanical compression are much less obvious in cycle 50, which indicates that the pressed electrode structure relaxes to some extent during cycling. Indeed, the electrode thickness measured by post-mortem analysis after ten cycles shows that the porosity of the compressed electrodes increases noticeably, as shown in
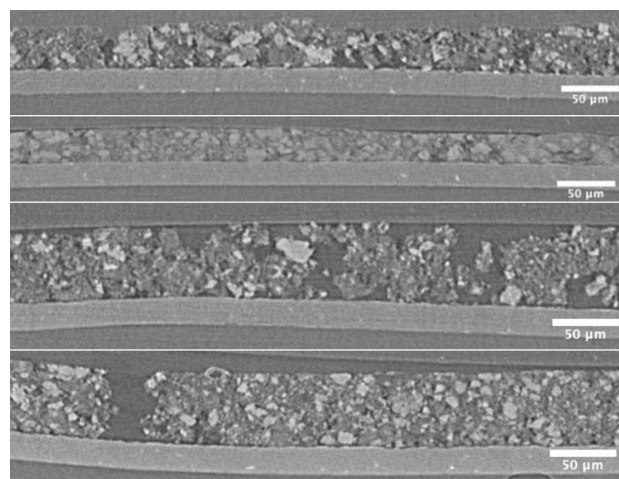

Figure 5. Cross-sections through the x-ray tomography image volumes parallel to the thickness direction. From top to bottom, the images are from pristine and compressed electrodes with a sulfur-loading of 2.0–2.5 $mg_S\,cm^{-2}$, and pristine and compressed electrodes with a sulfur-loading of 3.0–3.5 $mg_S\,cm^{-2}$. The Al current collector can be seen as a light grey layer under each electrode.

Table S3. The relaxation of the electrode structure may be caused by swelling binders[24] and/or the volume change

caused by precipitation and dissolution of elemental sulfur and Li$_2$S.[25] Nevertheless, Table S3 shows that, after cycling, the porosity of the compressed electrodes still remains higher than that of the pristine electrodes, and this is confirmed by the fact that the diffusion resistance also remains higher (Figure 3).

In cycle 100, where the pristine and mildly pressed electrodes start to show rapidly decreasing CE and discharge capacity, the voltage profiles exhibit an extended upper charge plateau, which is a feature of the redox shuttle between the positive and negative electrodes enabled by the dissolved polysulfides.[28] The intensified effect of polysulfide shuttling indicates the deterioration on the solid-electrolyte interphase (SEI) on the metallic lithium electrode, which is often attributed to the depletion of the electrolyte co-salt LiNO$_3$.[29–31] Although more investigation is required to conclude the causality, the onset of the intensified polysulfide shuttle is delayed in the cell with the electrode pressed at 108 MPa.

A substantially stronger impact of the porosity reduction on the internal and diffusion resistances is found in the electrodes with the higher sulfur-loading, as depicted in Figure 4. In the second cycle, the lower discharge plateau of the electrode with 37% porosity is shortened to less than half of that of the pristine electrode due to the high internal and diffusion resistances. Although these effects are reduced in the subsequent cycles, as also seen with the thinner electrodes, the resistance of the heavily pressed electrode is still more than twice as high as that of the other electrodes, which is distinct from the trend observed from the thinner electrodes. This suggests that the impact of compression on the electrode structure depends on the sulfur-loading, which is proportional to the thickness of the electrode given a fixed coating recipe.

To investigate why the sulfur-loading produces such strong effect on the resistance increase in the compressed electrodes, EIS and XRCT measurements were utilized to quantify the tortuosity of the electrodes before and after compression at
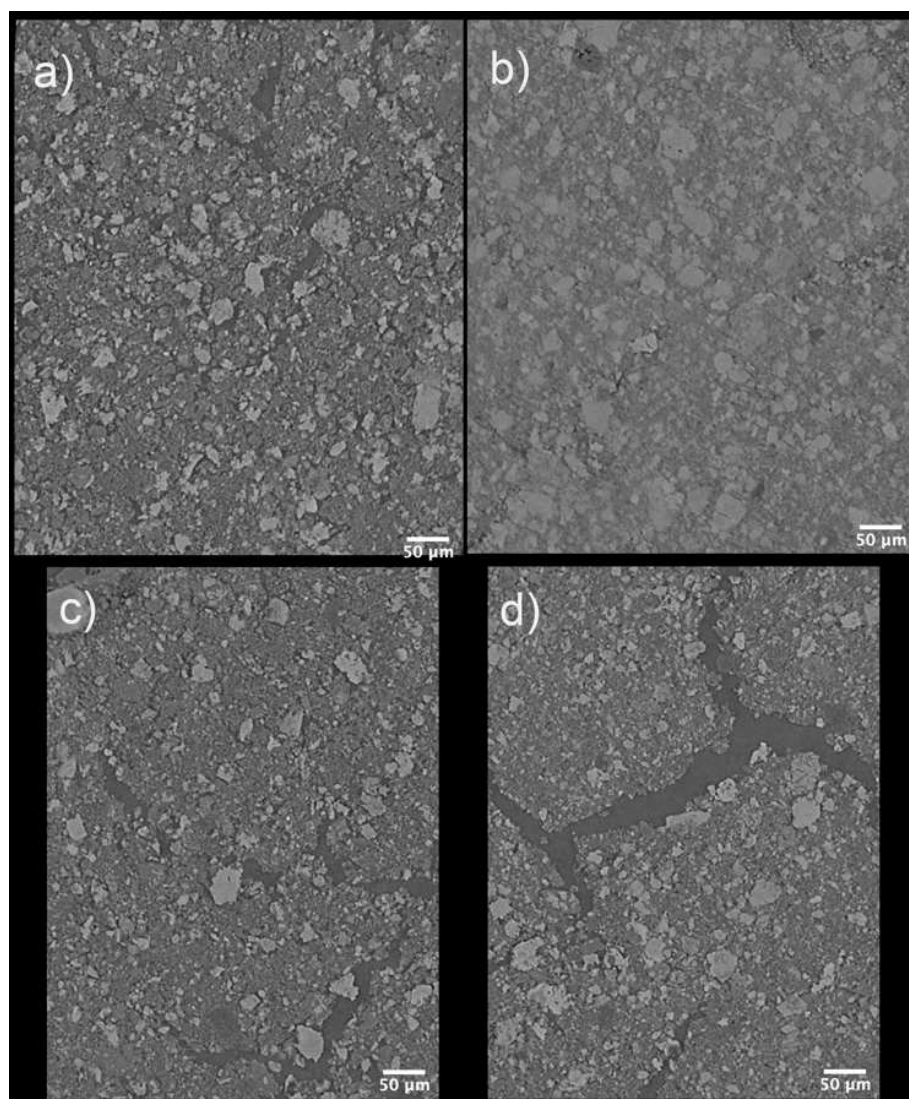

Figure 6. Cross-sections through the X-ray tomography image volumes perpendicular to the thickness direction. The images are from a) pristine and b) compressed electrodes with a sulfur-loading of 2.0–2.5 mg$_S$ cm^{-2} and c) pristine and d) compressed electrodes with a sulfur-loading of 3.0–3.5 mg$_S$ cm^{-2}.
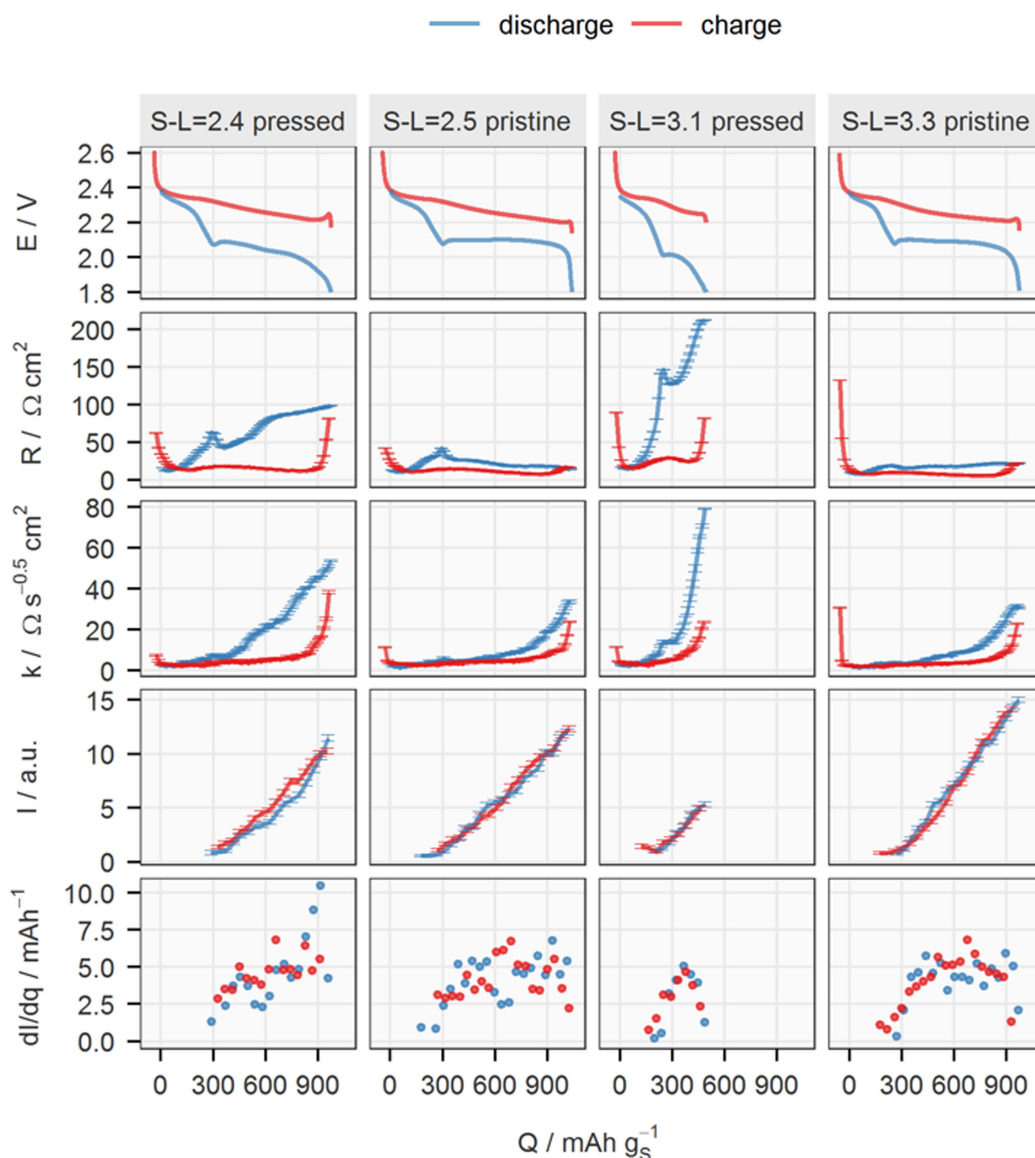
Figure 7. Summary of operando X-ray diffraction results from four cells with pristine and compressed electrodes at both sulfur-loading (S-L) ranges. Cell voltage (E), internal resistance (R), diffusion resistance coefficient (k), normalized integrated intensity under the 111 reflection of Li_2S (I) and its rate of changing with respect to the total charge passing through the cell (dI/dq) are plotted as a function of state of charge/discharge in terms of specific capacity (Q). The plots in each column share the same x-axis at the bottom. The data of the cells with pristine electrodes are obtained from the dataset of previous work.[34] The dI/dq values are smoothed by taking the average of three consecutive data points. The data presented here are from the 5th cycle of each operando XRD experiment.

108 MPa, as shown in Table 1. As explained in more detail in Section 9 of the Supporting Information, the tortuosity factors measure how the ionic transport is slowed down by the tortuous pathway in a porous electrode. Table 1 shows that the same trend in tortuosity factors is captured by both methods, but the exact values are smaller for the tortuosity factors derived from the image-based method, as found in previous studies.[30,31] Interestingly, both methods also consistently render a smaller tortuosity factor for the thicker compressed electrodes, compared to the thinner ones. This result is counterintuitive considering the higher value of resistance, specifically the diffusion resistance coefficient, of the com-

pressed electrodes with the higher loading, as demonstrated in Figures 3 and 4.

The mismatch between the changes in cell resistance and tortuosity factors is explained by further examination of the XRCT images. The cross-sections parallel to the thickness direction of the pristine and heavily compressed (108 MPa) electrodes at two sulfur-loadings are shown in Figure 5. The brightness in the XRCT data represents the x-ray attenuation and the sulfur filled carbon particles are the brightest, followed by the other carbon components and polymeric binders, leaving the voids as the darkest area. The effect of mechanical compression is manifested by the more condensed structure at both sulfur-loadings. However, there are obvious vertical void

Batteries & Supercaps

Research Article
doi.org/10.1002/batt.202200058

Chemistry
Europe
European Chemical
Societies Publishing

channels in the compressed thicker electrode, but not in the compressed thinner electrode. This distinction is more pronounced in the cross-sections perpendicular to the thickness direction in Figure 6, where a continuous void (~20 μm wide) can be observed in the compressed electrode with the higher sulfur-loading in Figure 6d. The formation of such wide voids may stem from the narrower voids (~10 μm wide) in the pristine electrode with the higher sulfur-loading, as displayed in Figure 6c. While these vertical gaps can explain the lower tortuosity of the compressed thicker electrode in comparison to that of the thinner one, such cracks have been reported to degrade the performance of electrodes in Li-ion batteries. For the Li-S system, it is reasonable to assume that the cracks have a negative influence on the kinetics of the redox reactions of the sulfur species because such damage of the carbon matrix renders the carbon particles susceptible to detachment when the electrode experiences volume change as sulfur species dissolve and precipitate repeatedly. The loss of conductive surface area of the carbon matrix leads to both higher charge-transfer resistance and worse transport properties inside the remaining porous electrode, which is reflected by the higher diffusion resistance coefficient, as seen for the electrode with 37% porosity in Figure 4.

To verify the hypothesis on the influence of the large voids on the kinetics of discharge and charge processes, a series of operando XRD measurements were carried out on the compressed electrodes at both sulfur-loadings and compared to the results obtained from the pristine electrodes in the previous study.[32] In Figure 7, except for about $20\,\Omega\,cm^2$ increase in the internal resistance, which may be introduced by the modifications on the coin cells for X-ray transmission, it can be seen that the trends in the voltage and resistance profiles of the operando XRD cells are comparable to the cells in Figures 3 and 4. From the integrated intensity of the 111 reflection of Li_2S in the fourth row of Figure 7, it can be inferred that in the compressed electrode with the higher sulfur-loading ('S-L = 3.1 pressed'), only one third of amount of the precipitate is found in comparison to the case in the thicker pristine electrode ('S-L = 3.3 pristine'). In contrast, the amount of Li_2S at the end of discharge in the pressed thinner electrode ('S-L = 2.4 pressed') is only slightly lower than in its pristine counterpart ('S-L = 2.5 pristine'). The intensity-to-charge ratio (dI/dq) analysis shows that the electrode structure of the pressed thicker electrode cannot sustain a precipitation rate of $5\,mAh^{-1}$ that is found on the lower discharge plateau in all other cells. The precipitation rate in the compressed thicker electrode starts to decrease when its diffusion resistance increases drastically, which indicates transport limitations in the discharge reaction.[24,33] This corroborates the above rationale of the negative effect of large voids in the compressed electrode, despite its lower tortuosity factor compared to the compressed electrode without large voids.

Conclusion

This work demonstrates mechanical compression as an effective way to manufacture S/C composite electrodes with high capacity density for tackling one of the biggest drawbacks of Li-S batteries, its low energy density. The capacity density of the S/C composite electrodes with sulfur-loading ranging from 2.0 to $3.5\,mg_S\,cm^{-2}$ can be doubled by applying a normal pressure of 108 MPa at 50 °C. The impact of the compression on the electrochemical properties of the S/C electrodes, namely internal and diffusion resistances, is characterized during cell operation for the first time. Although the compressed electrode structure is found to be relaxed along cycling, the cycling stability is still improved in the heavily compressed electrodes. The increase in the tortuosity factor accompanied by the lowered porosity in the as-pressed electrodes is quantified by both the symmetric cell method via electrochemical impedance spectroscopy and the restricted diffusion method via three-dimensional image from X-ray computed tomography. Both methods render a consistent trend in tortuosity, which contradicts the higher diffusion resistance measured during constant-current cycling in the thicker compressed electrodes. A combination of the tomographic results and a series of operando X-ray diffraction reveals that the μm-scale void channels formed in the thicker compressed electrodes can lower the tortuosity of the electrode structure, but the heterogenous density distribution is not ideal for mass transport during the precipitation of Li_2S. This study on the electrode structure thereby highlights the complexity and uniqueness of the Li-S system, compared to the insertion Li-ion electrode materials. The characterization methodologies and their results shed light on the correlation between electrode structure and electrochemical performance, to support the upcoming development of Li-S cells with high energy density.

Experimental Section

Materials

Elemental sulfur powder (S, Sigma-Aldrich), Ketjenblack (KB, EC-600JD, Akzo Nobel), Super C65 (C65, Imerys), carbon nanofibers (CNF, 20–200 nm×100 μm, Sigma-Aldrich), poly(ethylene oxide) (PEO, M_w~4000000, Sigma-Aldrich), poly(vinylpyrrolidone) (PVP, M_w~360000, Sigma-Aldrich), C-coated Al-foil (20 μm thick, SDX, Showa Denko), beryllium discs (Be, 99+%, ø16 mm, 0.25 mm thick, American Elements), Al-coated polyimide (25 μm coated with 30 nm Al on one side, Goodfellow), coin cells (CR2025, Hohsen) and hot-melting tape (thermo bonding film, Maskin & Verktyg, Sweden) were used as received. Lithium metal foil (Li, 125 μm thick, Cyprus Foote Mineral) was also used as received but stored under Ar atmosphere. Lithium bis(trifluoromethanesulfonyl)imide (LiTFSI, BASF) and lithium nitrate ($LiNO_3$, Sigma-Aldrich) were dried at 120 °C under vacuum for 12 h. 1,2-Dimethoxyethane (DME, BASF) and 1,3-dioxolane (DOL, Sigma-Aldrich) were dried using 3 Å molecular sieves for at least 12 h. Celgard® 2400 separators were dried under vacuum at 80 °C for 8 h.

Batteries & Supercaps

Research Article
doi.org/10.1002/batt.202200058

Chemistry Europe
European Chemical
Societies Publishing

Electrode preparation

The pristine S/C composite electrodes were made by coating the electrode slurry with a doctor blade. Based on a previously optimized recipe,[35] the slurry consists of 65% S, 21% KB, 3.5% C65, 3.5% CNF, 5.4% PEO and 1.6% PVP by mass. S was infused into KB by mixing in a mortar and then heating to 155°C for 20 min. After cooling down to room temperature, the mixture and the rest of the components were put into a ball mill jar with 20 vol% isopropanol solution in deionized water. After 2 h in a planetary ball mill, the mixture became a homogeneous slurry and was coated on the C-coated Al foil with two gap-settings on the doctor blade corresponding to two targeted sulfur loadings. After drying under atmospheric conditions, the coatings were cut into ø13 mm discs. The sulfur content in the electrode was confirmed by thermal gravimetric analysis (TA Instrument), as displayed in Figure S5.

The compression of the electrodes was conducted by a hydraulic press with heating function (YLJ-HP60-LD, MTI). One electrode is placed between two polished steel pellets (ø20 mm) at a time. For the electrodes pressed at 50°C, which are all the electrodes in the main text, the pellets and electrode were left in contact with both top and bottom plates of the press for 5 min for thermal equilibrium, which is skipped for pressing at room temperature for some electrodes presented in the Supporting Information. Either 108 or 54 MPa (based on the area of the electrodes) was applied by the hydraulic press for 1 min to complete the compression procedure. With the following equation, the porosity (ε) of the electrodes were calculated from the apparent volume (V_a), derived from the thickness measured by a micrometer, and the theoretical dense volume without pores (V_d), calculated from their mass and the density of the ingredients, which are listed in Table S4.

$$\varepsilon = \frac{V_a - V_d}{V_a} \#(1)$$

The physical properties measured for the calculation of the porosity and sulfur-loading of each electrode used in this manuscript are listed in Table S1.

Constant-current cycling and resistance measurements

All the S/C electrodes were dried in vacuum at 55°C for 12 h before assembly as a CR2025 coin cell with Celgard® 2400 separator (ø17 mm), Li metal disc (ø15 mm) and 6 µL mg$_s^{-1}$ of 1 M LiTFSI 0.25 M LiNO$_3$ DME:DOL (1:1, v:v) as the electrolyte. After a 6 h rest, the cells were discharged at C/50 (1 C = 1672 mAh g$_s^{-1}$) to 1.9 V and then charged at C/25 to 2.6 V in the first cycle. Afterwards, the cells were cycled at C/10 between 1.8 and 2.6 V. Every 5 min during the galvanostatic cycling, the current is paused for 1 s where the voltage response of the cell is recorded every 0.1 s, following the Intermittent Current Interruption (ICI) method.[24,36] It has been demonstrated in the previous work that the potential change ($\triangle E$) of a porous electrode or a diffusion-controlled reaction during a limited period after the constant current (I) is switched off can be expressed as the follows.[22,23,37]

$$\Delta E = -I(R + kt^{0.5}) \#(2)$$

where t is time since the current is off, R is the internal resistance and k is the diffusion resistance coefficient. By performing linear regression of $-\triangle E/I$ against $t^{0.5}$, R and k can be derived as the intercept and the slope. For a Li-S cell, R is a sum of electronic, solution and charge-transfer resistances while k characterizes the diffusion processes and/or transport properties of the porous carbon matrix.[25] The repetitive linear regression of each current

pause is conducted automatically by a script written in the R-programming language, which can be found with the electrochemical data via Zenodo data deposit.[38] The electrochemical test described above was carried out by an Arbin BT-2043 battery tester.

Determination of tortuosity factor by EIS on symmetric cells

For EIS characterisation, Swagelok-type symmetric cells were made with two electrodes (ø10 mm) from the same category (sulfur-loading and preparation process), two Whatman® GF/F separators (ø12 mm) and 120 µL 1 M LiTFSI 0.25 M LiNO$_3$ DME:DOL (1:1, v:v), following the procedure reported in previous works.[39,40] Copper rods and caps in contact with the electrodes were polished with 0.05 µm alumina powder in the final step and dried with the stainless steel cell body and Mylar film for aligning and insulating the electrode stack. Cells were rested for 6 h before the potential-controlled EIS measurements were performed with a voltage amplitude of 10 mV in the frequency range of 200 kHz to 10 mHz by a Bio-Logic VMP potentiostat. The spectra were then fitted using the software ZView to the equivalent circuit model (Scheme S1) containing an open Warburg element, whose coefficient (W) is used for calculating the tortuosity factor (τ) with the following equation.

$$\tau = \frac{k_{bulk}\varepsilon}{k_{pore}} = \frac{k_{bulk}\varepsilon}{\frac{d}{AW}} \#(3)$$

where k_{bulk} is the ionic conductivity of the bulk electrolyte, k_{pore} is the ionic conductivity of the electrolyte filled in the porous electrode, ε is the average porosity of the two tested electrodes, d is the sum of their thickness and A is the electrode area.

Determination of tortuosity factor by XRCT images

For X-ray computed tomography, rectangular electrode samples (1 mm × 1 mm^2) were cut from the electrodes by scissors with ceramic tips. Tomography was conducted using a Zeiss XRadia Versa XRM520 with a polychromatic cone beam operating at 50 kV and 4 W with the manufacturer supplied Le2 source filter and the 20× objective. 2001 projections were acquired, with an exposure time of 13 s per projection, over 360° to image internal regions of the electrodes. Tomographic reconstruction was performed using the Zeiss reconstructor software to yield 3D image volumes with cubic voxels of side length 670 nm. Cross-sectional images parallel and vertical to the thickness direction (Figures 5 and 6, respectively) were obtained with image processing software ImageJ from the three-dimensional image sequences.

For the evaluation of tortuosity factors with X-ray tomography data, the three-dimensional image sequence of the electrode coating was first cropped out and then binarized. The threshold was set to match the calculated porosity with the porosity calculated from thickness and mass measurement before the preparation of the tomography sample. The software Taufactor (version 1.1) was then used to calculate the tortuosity factor by diffusion simulation in the thickness direction of the electrode.[41,42]

Operando X-ray diffraction

Operando X-ray diffraction (XRD) data of the pristine electrodes were obtained from the published dataset[34] of the previous article.[32] The operando XRD measurements of the compressed electrodes follow the same method. The modified coin cells with X-ray transparent window (Al-coated polyimide) and spacers (Be

Batteries & Supercaps

Research Article
doi.org/10.1002/batt.202200058

Chemistry Europe
European Chemical
Societies Publishing

discs), which is illustrated in detail in the previous work, were made with compressed S/C electrodes while the rest of the cell components were the same as the standard coin cells made for constant-current cycling. XRD measurements were conducted on a STOE STADI P diffractometer in transmission mode with mono-chromatized Cu–Kα_1 radiation (45 kV, 40 mA). The patterns were collected for 903 s by a detector system comprised of three stationary Dectris Mythen 1 K strip detectors (~18° apart), covering an angular 2θ range from 0° to 54.8° with an angular resolution of 0.015° (2θ). The same constant-current cycling protocol with intermittent transient pauses were conducted by either an SP-150 or SP-240 (Bio-Logic) portable potentiostat. The evolution of the Li_2S species was characterized by modeling the Li_2S 111 reflection (Fm-3 m) using a single Gaussian peak whose intensity and width were refined with its position constrained to a 24°–29° (2θ) angular range with Topas Academic (V6) software.[43] A fourth degree Chebychev polynomial was used to model the background. In order to facilitate a comparison between the different cells, the intensity of the Li_2S 111 reflection was normalized to the 002 reflection of the polyimide film used as windows for the operando cell, thereby serving as an internal standard.

Acknowledgements

Conflict of Interest

The authors declare no conflict of interest.

Data Availability Statement

The data that support the findings of this study are available from the corresponding author upon reasonable request.

[1] W. Xue, L. Miao, L. Qie, C. Wang, S. Li, J. Wang, J. Li, *Curr. Opin. Electrochem.* **2017**, *6*, 92–99.
[2] P. Bonnick, E. Nagai, J. Muldoon, *J. Electrochem. Soc.* **2018**, *165*, A6005–A6007.
[3] P. Bonnick, J. Muldoon, *Energy Environ. Sci.* **2020**, *13*, 4808–4833.
[4] MIT Energy Initiative, *Insights into Future Mobility*, Cambridge, MA, **2019**.
[5] E. J. Berg, S. Trabesinger, *J. Electrochem. Soc.* **2018**, *165*, A5001–A5005.
[6] M. A. Pope, I. A. Aksay, *Adv. Energy Mater.* **2015**, *5*, 1–22.
[7] J. B. Robinson, K. Xi, R. V. Kumar, A. C. Ferrari, H. Au, M.-M. Titirici, A. Parra-Puerto, A. Kucernak, S. D. S. Fitch, N. Garcia-Araez, Z. L. Brown, M. Pasta, L. Furness, A. J. Kibler, D. A. Walsh, L. R. Johnson, C. Holc, G. N. Newton, N. R. Champness, F. Markoulidis, C. Crean, R. C. T. Slade, E. I. Andritsos, Q. Cai, S. Babar, T. Zhang, C. Lekakou, N. Kulkarni, A. J. E. Rettie, R. Jervis, M. Cornish, M. Marinescu, G. Offer, Z. Li, L. Bird, C. P. Grey, M. Chhowalla, D. di Lecce, R. E. Owen, T. S. Miller, D. J. L. Brett, S. Liatard, D. Ainsworth, P. R. Shearing, *J. Phys. Energy* **2021**, *3*, 031501.
[8] "OXIS Li-S Ultra-Light Cell," can be found under https://oxisenergy.com/products/, **2022**.
[9] K. H. Wujcik, D. R. Wang, A. A. Teran, E. Nasybulin, T. A. Pascal, D. Prendergast, N. P. Balsara, in *Electrochemical Engineering*, John Wiley & Sons, Ltd, **2018**, pp. 41–74.
[10] K. Xi, D. He, C. Harris, Y. Wang, C. Lai, H. Li, P. R. Coxon, S. Ding, C. Wang, R. V. Kumar, *Adv. Sci.* **2019**, *6*, 1–9.
[11] W. Xue, Z. Shi, L. Suo, C. Wang, Z. Wang, H. Wang, K. P. So, A. Maurano, D. Yu, Y. Chen, L. Qie, Z. Zhu, G. Xu, J. Kong, J. Li, *Nat. Energy* **2019**, *4*, 374–382.
[12] T. Wu, J. Qi, M. Xu, D. Zhou, Z. Xiao, *ACS Nano* **2020**, *14*, 15011–15022.
[13] J. Qi, T. Wu, M. Xu, Z. Xiao, *ACS Appl. Mater. Interfaces* **2021**, *13*, 39186–39194.
[14] C. Luo, E. Hu, K. J. Gaskell, X. Fan, T. Gao, C. Cui, S. Ghose, X. Yang, C. Wang, *Proc. Natl. Acad. Sci. USA* **2020**, *117*, 14712–14720.
[15] Z.-Q. Jin, Y.-G. Liu, W.-K. Wang, A.-B. Wang, B.-W. Hu, M. Shen, T. Gao, P.-C. Zhao, Y.-S. Yang, *Energy Storage Mater.* **2018**, *14*, 272–278.
[16] C. D. Reynolds, P. R. Slater, S. D. Hare, M. J. H. Simmons, E. Kendrick, *Mater. Des.* **2021**, *209*, 109971.
[17] C. Meyer, M. Weyhe, W. Haselrieder, A. Kwade, *Energy Technol.* **2020**, *8*, 1900175.
[18] A. C. Ngandjong, T. Lombardo, E. N. Primo, M. Chouchane, A. Shodiev, O. Arcelus, A. A. Franco, *J. Power Sources* **2021**, *485*, 229320.
[19] C. Meyer, M. Kosfeld, W. Haselrieder, A. Kwade, *J. Energy Storage* **2018**, *18*, 371–379.
[20] C.-S. Kim, A. Guerfi, P. Hovington, J. Trottier, C. Gagnon, F. Barray, A. Vijh, M. Armand, K. Zaghib, *J. Power Sources* **2013**, *241*, 554–559.
[21] P.-Y. Zhai, J.-Q. Huang, L. Zhu, J.-L. Shi, W. Zhu, Q. Zhang, *Carbon* **2017**, *111*, 493–501.
[22] Y.-C. Chien, A. S. Menon, W. R. Brant, D. Brandell, M. J. Lacey, *J. Am. Chem. Soc.* **2020**, *142*, 1449–1456.
[23] Y.-C. Chien, D. Brandell, M. J. Lacey, *Chem. Commun.* **2022**, *58*, 705–708.
[24] M. J. Lacey, F. Jeschull, K. Edström, D. Brandell, *J. Phys. Chem. C* **2014**, *118*, 25890–25898.
[25] P. Barai, A. Mistry, P. P. Mukherjee, *Extreme Mech. Lett.* **2016**, *9*, 359–370.
[26] Y. V. Mikhaylik, J. R. Akridge, *J. Electrochem. Soc.* **2004**, *151*, A1969.
[27] M. J. Lacey, A. Yalamanchili, J. Maibach, C. Tengstedt, K. Edström, D. Brandell, *RSC Adv.* **2016**, *6*, 3632–3641.
[28] S. S. Zhang, *Electrochim. Acta* **2012**, *70*, 344–348.
[29] D. Aurbach, E. Pollak, R. Elazari, G. Salitra, C. S. Kelley, J. Affinito, *J. Electrochem. Soc.* **2009**, *156*, A694–A702.
[30] J. Landesfeind, J. Hattendorff, A. Ehrl, W. A. Wall, H. A. Gasteiger, *J. Electrochem. Soc.* **2016**, *163*, A1373–A1387.
[31] J. Landesfeind, M. Ebner, A. Eldiven, V. Wood, H. A. Gasteiger, *J. Electrochem. Soc.* **2018**, *165*, A469–A476.
[32] Y.-C. Chien, A. S. Menon, W. R. Brant, M. J. Lacey, D. Brandell, *J. Phys. Chem. C* **2022**, *126*, 2971–2979.
[33] Y.-C. Chien, M. J. Lacey, N.-J. Steinke, D. Brandell, A. R. Rennie, *Chem* **2021**, DOI: 10.1016/j.chempr.2022.03.001.
[34] [dataset] Y.-C. Chien, A. S. Menon, W. R. Brant, M. J. Lacey, D. Brandell, **2022**, "Supporting data for 'Understanding the impact of precipitation kinetics on the electrochemical performance of lithium-sulfur batteries by operando X-ray diffraction,'" Zenodo, DOI: 10.5281/zenodo.5724078.
[35] M. J. Lacey, V. Österlund, A. Bergfelt, F. Jeschull, T. Bowden, D. Brandell, *ChemSusChem* **2017**, *10*, 2758–2766.
[36] M. J. Lacey, *ChemElectroChem* **2017**, *4*, 1997–2004.
[37] Y.-C. Chien, H. Liu, A. S. Menon, W. R. Brant, D. Brandell, M. J. Lacey, *ChemRxiv.* **2021**, Preprint DOI: 10.33774/chemrxiv-2021-09srz.
[38] [dataset] Y.-C. Chien, H. Li, J. Lampkin, S. Hall, N. Garcia-Araez, W. R. Brant, D. Brandell, M. J. Lacey, **2022**, "Supporting data for 'Impact of compression on the electrochemical performance of the sulfur/carbon composite electrode in lithium-sulfur batteries,'" Zenodo, DOI: 10.5281/zenodo.6350706.
[39] R. Raccichini, L. Furness, J. W. Dibden, J. R. Owen, N. García-Araez, *J. Phys. Chem. C* **2018**, *165*, A2741–A2749.
[40] H. Li, J. Lampkin, Y.-C. Chien, L. Furness, D. Brandell, M. J. Lacey, N. Garcia-Araez, *Electrochim. Acta* **2022**, *403*, 139572.
[41] S. J. Cooper, A. Bertei, P. R. Shearing, J. A. Kilner, N. P. Brandon, *SoftwareX* **2016**, *5*, 203–210.
[42] T.-T. Nguyen, A. Demortière, B. Fleutot, B. Delobel, C. Delacourt, S. J. Cooper, *npj Comput. Mater.* **2020**, *6*, 123.
[43] A. A. Coelho, *J. Appl. Crystallogr.* **2018**, *51*, 210–218.